Theory of Semiconductor Quantum-Dot Laser Dynamics

Weng W. Chow and Stephan W. Koch

***Abstract*—A theory for describing nonequilibrium dynamics in a semiconductor quantum-dot laser is presented. This theory is applied to a microcavity laser with a gain region consisting of an inhomogeneous distribution of quantum dots, a quantum-well wetting layer, and injection pumped bulk regions. Numerical results are presented and the effects of spectral hole burning, plasma heating, and many-body effects are analyzed.**

***Index Terms*—Hot carrier, laser theory, nonequilibrium carrier dynamics, quantum-dot lasers, semiconductor lasers.**

I. Introduction

ONE OF THE interesting aspects of semiconductor quantum-dot lasers is their potential for fast dynamical response [1], [2]. Three factors generally determine dynamical properties in a semiconductor laser: 1) electrical parasitics; 2) carrier transport; and 3) carrier relaxation and radiative recombination [3]. Whereas, the modulation bandwidth in bulk and quantum-well lasers mainly depends on factors 1) and 2) [4], [5], the third factor 3) plays a greater role for quantum-dot lasers [6]–[8]. This is because carrier relaxation is generally slowed down for discrete energy levels, to the extent that nonequilibrium effects influence dynamical behavior [9], [10].

In the literature, the dynamical behavior of semiconductor lasers is investigated using a wide range of approaches. In terms of analytical sophistication, on the one end of the spectrum are simple models based on rate equations [5], [10]–[12]. Here, the simplification is a consequence of the assumption that intraband relaxation is sufficiently rapid to always ensure quasi-equilibrium conditions. As a result, such rate equation models cannot systematically account for essential details of the relaxation processes and nonequilibrium situations, in spite of modifications [8], [13], [14].

On the opposite end of the spectrum of approaches are quantum mechanical theories that treat intraband collision processes microscopically at the level of quantum kinetic equations. Such approaches have been carried out for bulk and quantum-well structures [15]–[17], and recently, extended to quantum-dot systems [18], [19]. Their implementation requires state-of-the-art numerical techniques and often supercomputing resources. In practice, the system dynamics can be tracked only for durations that are not much longer than typical intraband relaxation times, i.e., for less than a few picoseconds. Applying these approaches to study an injection laser [20], [21], where it is often necessary to track slow (gigahertz) and fast (10^2 GHz) components of the system's overall dynamical response, requires substantial amounts of CPU time and computer memory. As a consequence, comprehensive studies of parameter dependencies can become impractical.

This paper presents a theory that bridges the gap between the two types of approaches. The result is a microscopically consistent description of a quantum-dot laser, that allows one to perform parametric studies of nonequilibrium effects on time scales ranging from subpicosecond to nanoseconds. This is accomplished using a semiclassical approach, where the laser field and active medium are described by the Maxwell–semiconductor–Bloch equations [22]. Many-body Coulomb effects, which we will show in this paper to be crucial for understanding microcavity quantum-dot laser dynamics [23], [24], are described at the level of the screened Hartree–Fock approximation. Carrier–carrier [25] and carrier–phonon [26] collisions are treated with the effective relaxation rate approximation, with the effective rates estimated from the quantum mechanical approach [18], [19], [27], [28].

While this separate treatment of screened Hartree–Fock and collisional effects is less rigorous than the full quantum kinetic theory, one gains from significantly reduced numerical demands in terms of the complexity and number of coupled differential equations. As a consequence, one can afford to treat other properties of the quantum-dot laser configuration in greater detail. For instance, in the description of current injection and carrier capture, the effects of the quantum-well and bulk states can be included and the influences of spectral-hole burning and state-filling on the inhomogeneously broadened quantum-dot distribution can be taken into account. Furthermore, the quantum-dot active medium treatment can be combined with the analysis of quite different optical arrangements. For example, the incorporation of the active medium model into a pump-probe configuration allows the modeling of time-resolved experiments yielding a consistent connection between the values of system parameters extracted from spectroscopy [7], [29], [30] and the dynamical performance observed in laser experiments [6], [31].

Details of our nonequilibrium quantum-dot laser theory are presented and discussed in Section II. Section III evaluates the capability of the theory to adequately reproduce carrier capture

Manuscript received September 14, 2004; revised November 8, 2004. The work of W. W. Chow was supported in part by Forschungspreis through the Alexander von Humboldt Foundation. The work of S. W. Koch was supported in part by the Max-Planck Research Prize of the Max-Planck Society and the Alexander von Humboldt Foundation. This work was partially funded by the U.S. Department of Energy under Contract DE-AC04-94AL8500 and the Deutsche Forschungsgemeinschaft.

W. W. Chow is with the Semiconductor Material and Device Sciences Department, Sandia National Laboratories, Albuquerque, NM 87185-0601 USA (e-mail: wwchow@sandia.gov).

S. W. Koch is with the Department of Physics and Material Sciences Center, Philipps University Marburg, 35032 Marburg, Germany.

Digital Object Identifier 10.1109/JQE.2005.843948

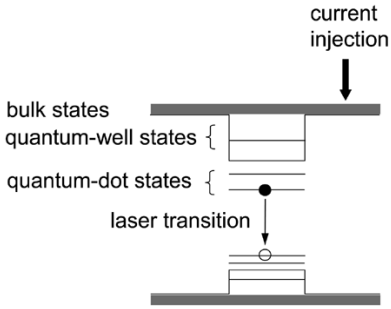

Fig. 1. Quantum-dot gain structure with quantum-dot (0-D), quantum well (2-D) and barrier (3-D) states for electrons and holes.

and relaxation processes, as described by a quantum kinetic approach. Here, we analyze the scenario where a high density of carriers is rapidly injected into the bulk region of a device, and examine the time evolution of optical and active medium properties. In Section IV, the theory is applied to a gain-switched laser, which is often studied using a rate-equation model. We examine the dependence of the laser dynamics on carrier capture and relaxation rates, showing explicitly the nonequilibrium deviations from rate equation results. Last, in Section V we calculate the modulation response of a quantum-dot laser in a wide range spanning 1–40 GHz.

II. Theory

The active quantum-dot-laser structure considered in our model is depicted in Fig. 1. It consists of bulk and quantum wells with embedded quantum dots. The quantum dots constitute the gain medium, which is inhomogeneously broadened due to the inhomogeneous size distribution of the dots in any realistic system. Under forward bias condition, carriers are injected into the bulk [three-dimensional (3-D)] electron and hole states. Some of the injected carriers are then transferred to quantum-well [two-dimensional (2-D)] states by intraband carrier–carrier and carrier–phonon collisions. The rest either remains in the bulk states, or is lost via electron–hole recombination and/or through drift and diffusion to the electrical contacts. Similarly, there is capture and relaxation between the quantum-well and the quantum-dot [zero-dimensional (0-D)] states. Since the quantum dots are the laser active medium, the carrier populations of the dot states also change by stimulated and spontaneous emission, as well as by nonradiative carrier losses.

In this paper, we mainly focus on the carrier capture and relaxation dynamics. So as not to be distracted by multimode behavior, such as mode hopping and competition, we assume a single-mode microcavity laser [23], [24]. Furthermore, we ignore all transverse field effects. In this limit, the laser field equation may be written as

$$E(z,t) = \frac{1}{2}\mathcal{E}(t)\, u(z) \exp(-i\omega t) + \text{c.c.} \tag{1}$$

where t is the time, z is the position along the laser axis, ω is the laser frequency, $u(z)$ is the passive resonator eigenfunction, and $\mathcal{E}(t)$ is a slowly varying complex electric field amplitude. The coupled laser field and gain medium may be described by the Maxwell–semiconductor–Bloch equations, which consist of the reduced wave equation for the laser field, and the semiconductor Bloch equations for the active region [22]. Starting with Maxwell's equations and using the slowly varying amplitude and phase approximation, the reduced wave equation (in MKS units) is

$$\frac{d\mathcal{E}(t)}{dt} = -\gamma_c \mathcal{E}(t) + \frac{i\omega\Gamma}{\varepsilon_b} P(t) \tag{2}$$

where γ_c is the cavity linewidth, ε_b is the background permittivity

$$\Gamma = \frac{n_{\text{qw}} w h}{w_f h_f} \tag{3}$$

is the optical mode confinement factor, n_{qw} is the number of quantum wells (with embedded dots) in the gain structure, w and h are the width and height of a quantum-well layer, and w_f and h_f are the laser beam width and height, respectively. In (2), $P(t)$ is the complex slowly varying polarization amplitude, defined for one of the quantum-well layers embedding the quantum dots. The connection between the classical optical properties and the quantum mechanical medium aspects of the problem is determined by the optical polarization

$$P(t) = \frac{N_d}{h} \sum_n \sum_{\alpha_n,\beta_n} \mu^*_{\alpha_n\beta_n} p_{\alpha_n\beta_n}(t) \tag{4}$$

where N_d is the quantum-dot density in each quantum-well layer and $p_{\alpha_n\beta_n}$ is the microscopic polarization amplitude. Here, we only include the polarization contributions from the dots since we assume that the quantum-well and bulk transitions are appreciably detuned from the laser field. As mentioned above, the quantum-dot distribution is inhomogeneously broadened because of dimensional or compositional fluctuations. We therefore denote the electron and hole states of the dots as α_n and β_n, where the subscript n labels that subgroup of quantum dots within the ensemble which has the same electron (hole) energies $\varepsilon_{e\alpha_n}$ $(\varepsilon_{h\beta_n})$ and the same dipole matrix element $\mu_{\alpha_n\beta_n}$.

The microscopic polarization amplitude $p_{\alpha_n\beta_n}$ is determined by solving the quantum mechanical semiconductor Bloch equations. For an active laser structure, these equations are derived using a Hamiltonian for the combined system of quantum dots and quantum well [32]

$$H = H_0 + H_{c-f} + H_C \tag{5}$$

where for the moment, we ignore the bulk layers. Equation (5) contains contributions from the free-carrier energy

$$H_0 = \sum_n \varepsilon_{\text{en}} a^\dagger_n a_n + \sum_m \varepsilon_{hm} b^\dagger_m b_m \tag{6}$$

the carrier–laser–field interaction energy

$$H_{c-f} = -\sum_{n,m} (\mu_{nm} a^\dagger_n b^\dagger_m + \mu^*_{nm} b_m a_n) E(z,t) \tag{7}$$

and the Coulomb interaction energy

$$H_C = \frac{1}{2}\sum_{n,m,r,s} W^{rs}_{nm} a^\dagger_r a^\dagger_s a_m a_n + \frac{1}{2}\sum_{n,m,r,s} W^{rs}_{nm} b^\dagger_r b^\dagger_s b_m b_n - \sum_{n,m,r,s} W^{rs}_{nm} a^\dagger_r b^\dagger_s b_m a_n. \tag{8}$$

Here, a_n and $a_n^\dagger$ are electron annihilation and creation operators, b_m and $b_m^\dagger$ are the corresponding operators for holes, and $\varepsilon_{\sigma n}$ is the free-carrier electron or hole energy. The subscripts and superscripts refer to either quantum-dot or well states, i.e., α_n or β_n for quantum-dot states, and $\sigma \mathbf{k}_\perp$ for quantum-well states, where $\sigma = e(h)$ for electrons (holes) and $\hbar \mathbf{k}_\perp$ is the in-plane carrier momentum. Equation (8) contains the Coulomb interaction energy matrix element

$$\begin{aligned} W_{nm}^{rs} &= \int d^2 r_1 \int d^2 r_2 \phi_r^*(\mathbf{r}_1)\phi_n(\mathbf{r}_1) W(\mathbf{r}_1 - \mathbf{r}_2) \\ &\quad \times \phi_s^*(\mathbf{r}_2)\phi_m(\mathbf{r}_2) \\ &= \sum_{\mathbf{q}\neq 0} W_q \int d^2 r_1 \phi_r^*(\mathbf{r}_1) e^{-i\mathbf{q}\cdot\mathbf{r}_1}\phi_n(\mathbf{r}_1) \\ &\quad \times \int d^2 r_2 \phi_s^*(\mathbf{r}_2) e^{-i\mathbf{q}\cdot\mathbf{r}_2}\phi_m(\mathbf{r}_2), \end{aligned} \tag{9}$$

where $\phi_n(\mathbf{r})$ is the dot or well wavefunction in the quantum-well plane

$$W_q = \frac{V_q}{\varepsilon_q} = \frac{1}{\varepsilon_q}\frac{e^2}{2A\varepsilon_b q} \tag{10}$$

is the Fourier transform of the screened Coulomb potential, V_q is the 2-D bare (unscreened) Coulomb potential, e is the electron charge, A is the area of the quantum well containing the quantum dots, and ε_q is the dielectric function describing screening by the electron–hole plasma in the quantum well. In our numerical evaluations, we evaluate ε_q using the plasmon-pole approximation of the Lindhard formula [22].

We proceed by working in the Heisenberg picture to derive the equations of motion for the microscopic polarization $p_{\alpha_n\beta_n} = \langle b_{\beta_n} a_{\alpha_n}\rangle$, electron population $n_{e\alpha_n} = \langle a_{\alpha_n}^\dagger a_{\alpha_n}\rangle$ and hole population $n_{h\beta_n} = \langle b_{\beta_n}^\dagger b_{\beta_n}\rangle$. In the screened Hartree–Fock limit [22], we obtain the following coupled equations [32]:

$$\begin{aligned} \frac{dp_{\alpha_n\beta_n}}{dt} &= -i\left(\omega_{\alpha_n\beta_n} - \omega\right) p_{\alpha_n\beta_n} \\ &\quad - i\Omega_{\alpha_n\beta_n}\left[n_{e\alpha_n} + n_{h\beta_n} - 1\right] + \left.\frac{\partial p_{\alpha_n\beta_n}}{\partial t}\right|_{\text{col}} \end{aligned} \tag{11}$$

$$\frac{dn_{e\alpha_n}}{dt} = \left[ip_{\alpha_n\beta_n}^*\Omega_{\alpha_n\beta_n} + \text{c.c.}\right] - \gamma_{\text{nr}}^d n_{e\alpha_n} + \left.\frac{\partial n_{e\alpha_n}}{\partial t}\right|_{\text{col}} \tag{12}$$

$$\frac{dn_{h\beta_n}}{dt} = \left[ip_{\alpha_n\beta_n}\Omega_{\alpha_n\beta_n} + \text{c.c.}\right] - \gamma_{\text{nr}}^d n_{h\beta_n} + \left.\frac{\partial n_{h\beta_n}}{\partial t}\right|_{\text{col}} \tag{13}$$

where the nonradiative and spontaneous emission carrier loss processes are approximated by the effective rate γ_{nr}^d. The terms $\partial/\partial t|_{\text{col}}$ represent the collision contributions described later in this section. To arrive at the above equations, we performed operator rearrangements using anticommutation relations for the carrier operators, and factorization of four-operator terms into two-operator terms that are very similar to those performed in the quantum-well and bulk derivations. The details of these manipulations may be found in several text books [22], [33].

Equations (11)–(13) contain contributions from many-body interactions via a renormalized transition energy

$$\begin{aligned} \hbar\omega_{\alpha_n\beta_n} &= \varepsilon_{e\alpha_n} - \varepsilon_{h\beta_n} - \sum_n W_{nn}^{\alpha_n\alpha_n} n_{\text{en}} \\ &\quad - \sum_m W_{mm}^{\beta_n\beta_n} n_{hm} + \sum_m \left(W_{mm}^{\beta_n\beta_n} - V_{mm}^{\beta_n\beta_n}\right) \end{aligned} \tag{14}$$

where $V_{mm}^{\beta_n\beta_n}$ is similar to (9) with W_q replaced by V_q. The summations in the above equation run over both quantum-well and quantum-dot states. The Hartree–Fock contributions also lead to a renormalization of the Rabi energy

$$\hbar\Omega_{\alpha_n\beta_n} = \frac{1}{2}\mu_{\alpha_n\beta_n}\mathcal{E}(t) + \sum_{n,m} W_{nm}^{\alpha_n\beta_n} p_{nm}. \tag{15}$$

Besides the screened Hartree–Fock contributions, the many-body interaction gives rise to collisions that lead to dephasing of the polarization and relaxation of the population distributions. As discussed in the introduction, it is very CPU-time consuming if one directly incorporates the microscopic, quantum-kinetic expressions for these collision effects into the numerical code used to treat the laser model. The scattering coefficients in the quantum kinetic treatment involve as many as five nested integrals over continuum states, and the phase space needed to track the carriers grows rapidly with integration time [18], [19], [27], [28]. In this paper, we explore an approximation using microscopic relaxation rates in the screened Hartree–Fock equations instead of solving the full equations. Since these relaxation rates are computed independent of the integration of the dynamic equations, this approach significantly reduces the numerical demands. In contrast to the usual effective rate treatment [5], [10]–[12], however, we retain enough features of the quantum kinetic treatment to adequately describe scattering effects under lasing conditions.

To proceed with our microscopic rate approximation scheme, we now examine the results from the full microscopic theory to identify the basic features of the relaxation processes which we then incorporate phenomenologically into our quantum-dot laser model. Take for example, polarization dephasing by collisons. The quantum kinetic treatment shows both diagonal and nondiagonal terms in $\partial p_{\alpha_n\beta_n}/\partial t|_{\text{col}}$ [22]. In bulk and quantum-well lasers, the nondiagonal contribution is important for correctly describing the lineshape of gain and absorption spectra over a wide frequency range. Hence, it is not sufficient to model dephasing by just taking the diagonal contribution. However, as long as one is interested in systems under lasing conditions, where the lasing frequency is close to gain peak and the intracavity carrier density does not deviate appreciably from the threshold value, one can approximate the combined effect of diagonal and nondiagonal dephasing by a simple rate. Generally, this rate has to be obtained by computing absorption/gain spectra including diagonal and nondiagonal dephasing and performing a best fit to the numerical result. In this spirit, we approximate the polarization dephasing term in our quantum-dot laser model [19]

$$\left.\frac{\partial p_{\alpha_n\beta_n}}{\partial t}\right|_{\text{col}} = -\gamma p_{\alpha_n\beta_n} \tag{16}$$

where γ is the effective dephasing rate [28].

For the equilibration of a nonequilibrium carrier distribution, we consider, for instance, the relaxation of a nonequilibrium electron distribution generated by an optical pulse that is resonant with a bulk state transition in our system. Immediately after the pump pulse, the electron populations in the quantum-dot, quantum-well and bulk states, $n_{e,\alpha_n}, n_{e,\mathbf{k}_\perp}$, and $n_{e,\mathbf{k}}$, respectively, are driven by collisions toward distributions described by Fermi–Dirac functions

$$f(\varepsilon,\mu,T)=\left[\exp\left(\frac{\varepsilon-\mu}{k_BT}\right)+1\right]^{-1} \tag{17}$$

where ε is the energy of the state, μ is the chemical potential, k_B is Boltzmann's constant and T is the temperature. The relaxation occurs on several characteristic time scales.

1) The fastest processes are carrier–carrier collisions involving continuous states in the bulk and quantum-well regions, i.e., in two (superscript 2) of the three subsystems (bulk, well, dot). These collisions drive the respective populations to quasi-equilibrium, so that

$$\{n_{e,\alpha_n},n_{e,\mathbf{k}_\perp},n_{e,\mathbf{k}}\}\rightarrow\{n_{e,\alpha_n},f\left(\varepsilon_{e,\mathbf{k}_\perp},\mu_e^{(2p)},T_{2p}\right),f\left(\varepsilon_{e,\mathbf{k}},\mu_e^{(2p)},T_{2p}\right)\} \tag{18}$$

where the label $2p$ indicates that the properties are associated with the plasma (p) in the bulk and the quantum-well regions. How $\mu_e^{(2p)}$ and T_{2p} are determined will be discussed later. Note that we use a common reference for all the energies and chemical potentials, which in this paper is the bottom of the quantum well.

2) On a slower time scale the carrier–phonon collisions relax the quasi-equilibrium distributions in the bulk and quantum-well regions from the temperature T_{2p} to the lattice temperature T_l

$$\{n_{e,\alpha_n},f\left(\varepsilon_{e,\mathbf{k}_\perp},\mu_e^{(2p)},T_{2p}\right),f\left(\varepsilon_{e,\mathbf{k}},\mu_e^{(2p)},T_{2p}\right)\}\rightarrow\{n_{e,\alpha_n},f\left(\varepsilon_{e,\mathbf{k}_\perp},\mu_e^{(2l)},T_l\right),f\left(\varepsilon_{e,\mathbf{k}},\mu_e^{(2l)},T_l\right)\} \tag{19}$$

where there is now a new chemical potential $\mu_e^{(2l)}$ for the quasi-equilibrium distributions, because of the temperature change.

3) The even slower collisions involving discrete quantum-dot states come into play. With the added effects of dot-dot and dot-well carrier–carrier scattering, we have

$$\{n_{e,\alpha_n},f\left(\varepsilon_{e,\mathbf{k}_\perp},\mu_e^{(2l)},T_l\right),f\left(\varepsilon_{e,\mathbf{k}},\mu_e^{(2l)},T_l\right)\}\rightarrow\{f\left(\varepsilon_{e,\alpha_n},\mu_e^{(3p)},T_{3p}\right),f\left(\varepsilon_{e,\mathbf{k}_\perp},\mu_e^{(3p)}T_{3p}\right),f\left(\varepsilon_{e,\mathbf{k}},\mu_e^{(3p)},T_{3p}\right)\} \tag{20}$$

where the label $(3p)$ indicates that the quantity is computed involving all three (dot, well, and bulk) regions.

4) Finally, from carrier–phonon collisions, we have

$$\{f\left(\varepsilon_{e,\alpha_n},\mu_e^{(3p)},T_{3p}\right),f\left(\varepsilon_{e,\mathbf{k}_\perp},\mu_e^{(3p)}T_{3p}\right),f\left(\varepsilon_{e,\mathbf{k}},\mu_e^{(3p)}T_{3p}\right)\}\rightarrow\{f\left(\varepsilon_{e,\alpha_n},\mu_e^{(3l)},T_l\right),f\left(\varepsilon_{e,\mathbf{k}_\perp},\mu_e^{(3l)},T_l\right),f\left(\varepsilon_{e,\mathbf{k}},\mu_e^{(3l)},T_l\right)\} \tag{21}$$

Based on the above phenomenological description of electron relaxation in our quantum-dot laser structure, and assuming that the process is similar for the hole populations, we write for the occupation in the quantum-dot states

$$\left.\frac{\partial n_{\sigma\alpha_n}}{\partial t}\right|_{\text{col}}=-\gamma_{c-c}^{(3)}\left[n_{\sigma\alpha_n}-f\left(\varepsilon_{\sigma\alpha_n},\mu_\sigma^{(3p)},T_{3p}\right)\right]-\gamma_{c-p}^{(3)}\left[n_{\sigma\alpha_n}-f\left(\varepsilon_{\sigma\alpha_n},\mu_\sigma^{(3l)},T_l\right)\right]-\gamma_{\text{nr}}n_{\sigma\alpha_n} \tag{22}$$

where $\gamma_{c-c}^{(3)}$ and $\gamma_{c-p}^{(3)}$ are the effective relaxation rates for relaxation of the entire (dot, well, and bulk) carrier population by carrier–carrier and carrier–phonon collisions, respectively. In addition, we include a nonradiative loss term with an effective rate of γ_{nr}. Similarly, the equation of motion for the quantum-well populations is

$$\frac{dn_{\sigma\mathbf{k}_\perp}}{dt}=-\gamma_{c-c}^{(2)}\left[n_{\sigma\mathbf{k}_\perp}-f\left(\varepsilon_{\sigma\mathbf{k}_\perp},\mu_\sigma^{(2p)},T_{2p}\right)\right]-\gamma_{c-c}^{(3)}\left[n_{\sigma\mathbf{k}_\perp}-f\left(\varepsilon_{\sigma\mathbf{k}_\perp},\mu_\sigma^{(3p)},T_{3p}\right)\right]-\gamma_{c-p}^{(2)}\left[n_{\sigma\mathbf{k}_\perp}-f\left(\varepsilon_{\sigma\mathbf{k}_\perp},\mu_\sigma^{(2l)},T_l\right)\right]-\gamma_{c-p}^{(3)}\left[n_{\sigma\mathbf{k}_\perp}-f\left(\varepsilon_{\sigma\mathbf{k}_\perp},\mu_\sigma^{(3l)},T_l\right)\right]-\gamma_{\text{nr}}^{\text{qw}}n_{\sigma\mathbf{k}_\perp} \tag{23}$$

and for the bulk populations

$$\frac{dn_{\sigma\mathbf{k}}}{dt}=-\gamma_{c-c}^{(2)}\left[n_{\sigma\mathbf{k}}-f\left(\varepsilon_{\sigma\mathbf{k}},\mu_\sigma^{(2p)},T_{2p}\right)\right]-\gamma_{c-c}^{(3)}\left[n_{\sigma\mathbf{k}}-f\left(\varepsilon_{\sigma\mathbf{k}},\mu_\sigma^{(3p)},T_{3p}\right)\right]-\gamma_{c-p}^{(2)}\left[n_{\sigma\mathbf{k}}-f\left(\varepsilon_{\sigma\mathbf{k}},\mu_\sigma^{(2l)},T_l\right)\right]-\gamma_{c-p}^{(3)}\left[n_{\sigma\mathbf{k}}-f\left(\varepsilon_{\sigma\mathbf{k}},\mu_\sigma^{(3l)},T_l\right)\right]+\Lambda_{\sigma\mathbf{k}}-\gamma_{\text{nr}}^{b}n_{\sigma\mathbf{k}} \tag{24}$$

where $\gamma_{c-c}^{(2)}$ and $\gamma_{c-p}^{(2)}$ are the effective relaxation rates for relaxation of the quantum-well and bulk carrier populations by carrier–carrier and carrier–phonon collisions, respectively, $\gamma_{\text{nr}}^{\text{qw}}$ and γ_{nr}^{b} are the effective nonradiative carrier loss rates.

The pump contribution is

$$\Lambda_{\sigma\mathbf{k}}(t)=\frac{J(t)}{eh_bN_{p,\sigma}}f\left(\varepsilon_{\sigma\mathbf{k}},\mu_\sigma^p,T_l\right)\left(1-n_{\sigma\mathbf{k}}\right) \tag{25}$$

where J is the injected current density, $f(\varepsilon_{\sigma\mathbf{k}},\mu_\sigma^p,T_l)$, h_b, and $N_{p,\sigma}$ are the steady state electron or hole distributions and density in the absence of a laser field, and the quantity $(1-n_{\sigma\mathbf{k}})$ accounts for pump blocking due to the exclusion principle [21].

Solving (11)–(13) with the relaxation contributions given by (22)–(24) requires knowing the Fermi–Dirac distributions at each time step. To determine these distributions in the different subsystems, we use the fact that the total electron and hole density is conserved in carrier–carrier collisions, such that

$$N_\sigma^d+N_\sigma^q+N_\sigma^b=n_{\text{qw}}N_{\text{dot}}\sum_n\sum_{\alpha_n}f\left(\varepsilon_{\sigma\alpha_n},\mu_\sigma^{(3p)},T_{3p}\right)+\frac{n_{\text{qw}}}{A}\sum_{\mathbf{k}_\perp}f\left(\varepsilon_{\sigma\mathbf{k}_\perp},\mu_\sigma^{(3p)},T_{3p}\right)+\frac{h_b}{V_b}\sum_{\mathbf{k}}f\left(\varepsilon_{\sigma\mathbf{k}},\mu_\sigma^{(3p)},T_{3p}\right) \tag{26}$$

where $N_{\rm dot}$ is the areal density of dots in each of the $n_{\rm qw}$ quantum-well layers and $\sigma = e$ or h, h_b is the thickness of the barrier region. Furthermore, we introduced the total sheet (2d) carrier densities in the quantum-dot, quantum-well, and bulk regions,

$$N_\sigma^d = n_{\rm qw} N_{\rm dot} \sum_n \sum_{\alpha_n} n_{\sigma,\alpha_n} \tag{27}$$

$$N_\sigma^q = \frac{n_{\rm qw}}{A} \sum_{\mathbf{k}_\perp} n_{\sigma,\mathbf{k}_\perp} \tag{28}$$

$$N_\sigma^b = \frac{h_b}{V} \sum_{\mathbf{k}} \varepsilon_{\sigma\mathbf{k}} n_{\sigma\mathbf{k}} \tag{29}$$

respectively.

Besides particle number conservation, the carrier–carrier collisions also conserve the total electron and hole kinetic energy, i.e.,

$$\begin{aligned} &n_{\rm qw} N_{\rm dot} \sum_n \sum_{\alpha_n} \varepsilon_{\sigma\alpha_n} n_{\sigma,\alpha_n} \\ &\quad + \frac{n_{\rm qw}}{A} \sum_{\mathbf{k}_\perp} \varepsilon_{\sigma\mathbf{k}_\perp} n_{\sigma,\mathbf{k}_\perp} + \frac{h_b}{V} \sum_{\mathbf{k}} \varepsilon_{\sigma\mathbf{k}} n_{\sigma\mathbf{k}} \\ &= n_{\rm qw} N_{\rm dot} \sum_n \sum_{\alpha_n} \varepsilon_{\sigma\alpha_n} f\left(\varepsilon_{\sigma\alpha_n}, \mu_\sigma^{(3p)}, T_{3p}\right) \\ &\quad + \frac{n_{\rm qw}}{A} \sum_{\mathbf{k}\perp} \varepsilon_{\sigma\mathbf{k}_\perp} f\left(\varepsilon_{\sigma\mathbf{k}_\perp}, \mu_\sigma^{(3p)}, T_{3p}\right) \\ &\quad + \frac{h_b}{V_b} \sum_{\mathbf{k}} \varepsilon_{\sigma\mathbf{k}} f\left(\varepsilon_{\sigma\mathbf{k}}, \mu_\sigma^{(3p)}, T_{3p}\right). \end{aligned} \tag{30}$$

In the case of carrier–phonon collisions, the total carrier density is conserved, while energy is exchanged between the carriers and lattice by the creation and annihilation of phonons. Therefore, the only requirement is

$$\begin{aligned} N_\sigma^d + N_\sigma^q + N_\sigma^b &= n_{\rm qw} N_{\rm dot} \sum_n \sum_{\alpha_n} f\left(\varepsilon_{\sigma\alpha_n}, \mu_\sigma^{(3l)}, T_l\right) \\ &\quad + \frac{n_{\rm qw}}{A} \sum_{\mathbf{k}_\perp} f\left(\varepsilon_{\sigma\mathbf{k}_\perp}, \mu_\sigma^{(3l)}, T_l\right) \\ &\quad + \frac{h_b}{V_b} \sum_{\mathbf{k}} f\left(\varepsilon_{\sigma\mathbf{k}}, \mu_\sigma^{(3l)} T_l\right) \end{aligned} \tag{31}$$

where the energy exchange between carriers and lattice is taken into account by fixing the temperature of the quasi-equilibrium distributions to the lattice temperature T_l.

For the situation where only the quantum-well and bulk populations are in quasi-equilibrium, the corresponding Fermi–Dirac distributions are determined from the conditions

$$\begin{aligned} N_\sigma^q + N_\sigma^b &= \frac{n_{\rm qw}}{A} \sum_{\mathbf{k}_\perp} f\left(\varepsilon_{\sigma\mathbf{k}_\perp}, \mu_\sigma^{(2p)}, T_{2p}\right) \\ &\quad + \frac{h_b}{V_b} \sum_{\mathbf{k}} f\left(\varepsilon_{\sigma\mathbf{k}}, \mu_\sigma^{(2p)}, T_{2p}\right) \end{aligned} \tag{32}$$

$$\begin{aligned} &\frac{n_{\rm qw}}{A} \sum_{\mathbf{k}_\perp} \varepsilon_{\sigma\mathbf{k}_\perp} n_{\sigma,\mathbf{k}_\perp} + \frac{h_b}{V} \sum_{\mathbf{k}} \varepsilon_{\sigma\mathbf{k}} n_{\sigma,\mathbf{k}} \\ &\quad = \frac{n_{\rm qw}}{A} \sum_{\mathbf{k}\perp} \varepsilon_{\sigma\mathbf{k}_\perp} f\left(\varepsilon_{\sigma\mathbf{k}_\perp}, \mu_\sigma^{(2p)}, T_{2p}\right) \\ &\quad\quad + \frac{h_b}{V_b} \sum_{\mathbf{k}} \varepsilon_{\sigma\mathbf{k}} f\left(\varepsilon_{\sigma\mathbf{k}}, \mu_\sigma^{(2p)}, T_{2p}\right) \end{aligned} \tag{33}$$

and

$$\begin{aligned} N_\sigma^q + N_\sigma^b &= \frac{n_{\rm qw}}{A} \sum_{\mathbf{k}_\perp} f\left(\varepsilon_{\sigma\mathbf{k}_\perp}, \mu_\sigma^{(2l)}, T_l\right) \\ &\quad + \frac{h_b}{V_b} \sum_{\mathbf{k}} f\left(\varepsilon_{\sigma\mathbf{k}}, \mu_\sigma^{(2l)}, T_l\right). \end{aligned} \tag{34}$$

We note that in the above description, the transport of carriers between the different regions is taken into account as an integral part of the capture and relaxation processes due to carrier–carrier and carrier–phonon collisions.

During the numerical computations, (26) and (30) yield $\mu_\sigma^{(3p)}$ and T_{3p}. Equations (32) and (33) are solved for $\mu_\sigma^{(2p)}$ and T_{2p}, (31) gives $\mu_\sigma^{(3l)}$, and (34) yields $\mu_\sigma^{(2l)}$. All the summations in these equations have to be evaluated numerically. The gauge we use to determine that the summations and the solutions are performed to the necessary accuracy is to examine the extent to which total (matter and radiation field) energy is conserved over the span of the calculation.

In the examples presented in the later sections of this paper we demand that the radiation field energy change by stimulated emission equals the energy change associated with changes in electron and hole populations to less than 2% at all times. It is necessary that (26)–(34) are solved to the accuracy that the left-hand side of each equation differs from the right-hand side by less than 0.0001%, which is quite stringent. For example to achieve this accuracy, we cannot use the analytic formula giving the chemical potential of a 2-D plasma as a function of the 2-D density [22], because of the inaccuracy associated with the numerical evaluation of logarithms. Roughly two thirds of the computation time in a run is spent determining the quasi-equilibrium functions.

The degree to which the rate approximation scheme is consistent with the results of fully microscopic calculations (e.g., [22, Figs. 4.2–4.5]) depends on the detailed situation considered in the simulation. In particular, the relevant configurations should not involve very large deviations from quasi-equilibrium. It is also desirable that the effective relaxation times are sufficiently different from one another so that the relaxation behavior shows distinct properties of the different stages described earlier. This is generally true with collisions involving the continuous quantum-well and bulk states, where the effective carrier–carrier relaxation rate $\gamma_{c-c}^{(2)}$ under lasing condition is an order of magnitude larger than the effective carrier–phonon relaxation rate $\gamma_{c-p}^{(2)}$ [16]. For the collisions involving discrete states, the effective rates $\gamma_{c-c}^{(3)}$ and $\gamma_{c-p}^{(3)}$ can be over an order of magnitude slower than $\gamma_{c-c}^{(2)}$ and $\gamma_{c-p}^{(2)}$ [9], [10], [18], [19].

To close this section, we explain the procedure used to determine the effective relaxation rates used in our simulations. For the bulk and quantum-well regions, we take the rates $\gamma_{c-c}^{(2)}$ and $\gamma_{c-p}^{(2)}$ that enable our model to best reproduce the microscopically calculated relaxation of a locally perturbed carrier distribution (spectral bump or hole) back to a Fermi–Dirac distribution. As shown in [28], one obtains good overall agreement even though at any given time during the relaxation process, there are slight differences in the shape of the spectral bump or hole. These differences, however, only marginally influence the nonequilibrium gain under the respective conditions. Typ-

ical room temperature effective relaxation rates extracted from microscopic calculations are approximately 1 to 2×10^{13} s^{-1} for carrier–carrier collisions, and approximately 0.2 to 1×10^{12} s^{-1} for carrier–phonon collisions [15], [16], [21], [28].

Unfortunately, a similarly systematic comparison between approximate and microscopic treatments for a quantum-dot structure is currently not possible because we still do not have a fully consistent numerical analysis of a complete microscopic model for the inhomogeneously broadened quantum-dot structure shown in Fig. 1. Without such a comparison, the effective relaxation rates $\gamma_{c-c}^{(3)}$ and $\gamma_{c-p}^{(3)}$ are obtained by using the real parts of the scattering coefficients in the second Born approximation for carrier–carrier and carrier–phonon collisions, respectively [18], [19]. Presently there is some uncertainty concerning these values within the range 10^{13} s^{-1} to 10^{11} s^{-1} for room temperature [18], [19]. Therefore, we present results for different rates.

III. Nonequilibrium Gain Effects

To evaluate the theory, we consider a single-mode laser operating with a gain structure consisting of five 3-nm-thick $In_{02}Ga_{0.8}As$ quantum-well layers, where each layer contains a density of 10^{11} cm^{-2} $In_{0.6}Ga_{0.4}As$ quantum dots. The quantum wells are separated by 6-nm GaAs barriers and the entire structure is cladded by $Al_{0.1}Ga_{0.9}As$ bulk layers. We approximate the quantum-dot shape by a 3-nm-high, 30-nm-diameter cylindrical disk. Using $\mathbf{k} \cdot \mathbf{p}$ theory and assuming separation of variables in growth and radial directions [34], the calculated electronic structure contains one electron and one hole quantum-dot bound state with 1.074 eV energy separation and $e \times 0.56$ nm dipole matrix element. Other input parameters are $\gamma = \gamma_{c-c}^{(2)} = 10^{13}$ s^{-1}, $\gamma_{c-p}^{(2)} = 10^{12}$ s^{-1} [28], and $\Gamma = 0.20$ mode confinement factor. A normal distribution is used to describe the inhomogeneous broadening in the quantum dots. For example, the quantum-dot carrier density is

$$N_\sigma^d = n_{\mathrm{qw}} N_{\mathrm{dot}} \sum_\alpha \int d\varepsilon \rho_\alpha(\varepsilon) n_{\sigma\alpha}(\varepsilon) \tag{35}$$

where

$$\rho_\alpha(\varepsilon) = \frac{1}{\sqrt{2\pi}\sigma_{\mathrm{inh}}} \exp\left[-\left(\frac{\varepsilon - \varepsilon_{\sigma\alpha}}{\sqrt{2}\sigma_{\mathrm{inh}}} \right)^2 \right] \tag{36}$$

$\varepsilon_{\sigma\alpha}$ is the average quantum-dot energy in the αth state. For the following calculations, we choose a standard deviation $\sigma_{\mathrm{inh}} = 30$ meV. We note that the present treatment of inhomogeneous broadening is an improvement over the often used statistical averaging of the homogeneously broadened results [35]. There, one generally assumes equal carrier density in ensemble, whereas here, the ensemble has the possibility to relax to a common chemical potential, where the system has a distribution of different carrier densities.

First, we wish to confirm that our theory can reasonably accurately reproduce features expected of the optical response under nonequilibrium conditions. For this test, we calculate the changes in laser output due a current spike. Initially, the laser is operating continuous wave (CW) at five times above threshold with injection current density $J = 600$ A/cm^2. The input parameters are those given in the previous paragraph together with $\gamma_{c-c}^{(3)} = 2 \times 10^{11}$ s^{-1} and $\gamma_{c-p}^{(3)} = 10^{11}$ s^{-1} for the scattering rates involving quantum-dot states [18], [19], and $\gamma_c = 10^{12}$ s^{-1} for optical resonator linewidth. The current pulse, which is chosen to accentuate nonequilibrium effects rather than for experimental practicality, peaks at $J = 6$ kA/cm^2 with 1 ps rise and fall times and 60-ps duration [dashed curve, Fig. 2(a)]. In Fig. 2(a), the solid curve shows the changes in laser output intensity, which has the following interesting features: 1) dip in intensity immediately after the onset of current pulse; 2) decrease in laser output prior to the end of the current pulse; and 3) appearance of a second optical pulse after termination of the current pulse. These features are consistent with the temporal behavior of the laser gain, as plotted in Fig. 2(b). Fig. 2(b) further shows the clamping of the steady-state gain at the optical resonator linewidth $\gamma_c = 10^{12}$ s^{-1}.

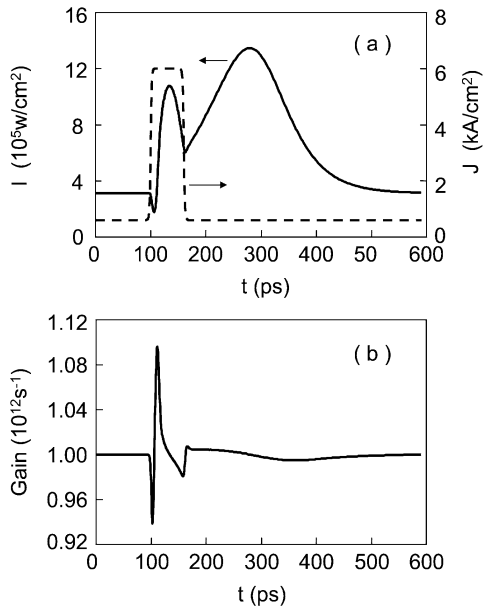

Fig. 2. Time dependence of (a) laser intensity and injection current and (b) laser gain.

An explanation for the laser dynamical behavior can be found in Figs. 3 and 4. First, Fig. 3(a) depicts the time dependence of the plasma temperature $T_p^{(3)}$, where we note an increase in plasma temperature immediately after the onset of the current pulse. This temperature increase is due to the thermalization of injected carriers via carrier–carrier scattering. Since carriers injected into the bulk layer have an energy above the quantum-dot and most quantum-well states, on the average, they lose energy during scattering. To conserve total energy, carriers in the quantum-dot and low-lying quantum-well states scatter into higher energy states. This redistribution of carriers has the effect of heating the plasma, which is a well known phenomenon in quantum kinetic treatments [20]. A higher temperature leads to lower gain [Fig. 2(b)], and consequently, lower laser intensity [solid curve, Fig. 2(a)].

Eventually, the laser output rises above its CW value. This increase can be attributed both to carrier–phonon scattering, which cools the plasma via energy transfer to the lattice, and to the ongoing increase in carrier density due to the continuing higher level of current injection. However, the laser output reaches a peak before the end of the current pulse. The subsequent decrease in laser output while the carrier density is still

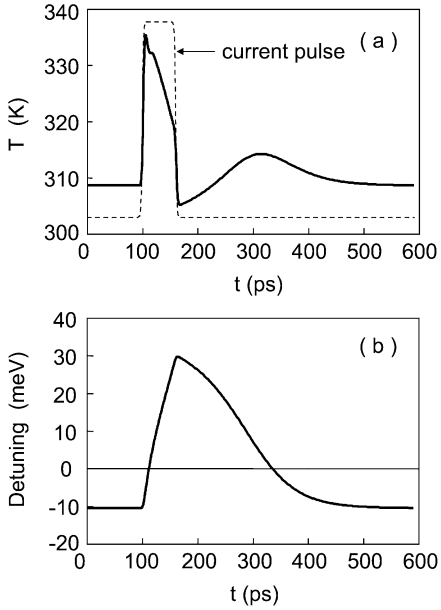

Fig. 3. Time dependence of (a) plasma temperature and (b) detuning.

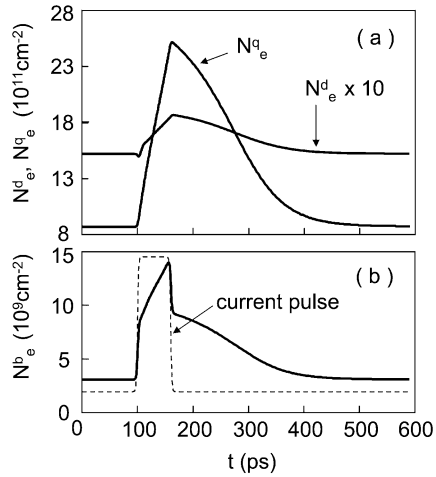

Fig. 4. Time dependence of electron populations in (a) the quantum-dot and quantum-well regions and (b) in the bulk part of the structure .

rising is caused by many-body effects. Fig. 3(b) is a plot of the detuning between the peak of the inhomogeneous quantum-dot distribution and the lasing energy. We picked a detuning that is approximately zero for CW operation, so that the laser operates at the gain maximum. Immediately after the onset of the current pulse, the increases in quantum-dot and quantum-well populations [Fig. 4(a)] change the many-body bandgap renormalization, which detunes the laser away from the gain maximum. Because we considered operation in a microcavity with optical resonances spaced apart wider than the quantum-dot inhomogeneous linewidth, the detuning leads to a decrease in the laser output instead of the mode hopping expected in a multimode laser.

Many-body effects are amplified over those in a quantum-well laser for two reasons. First, the rapid injection of carriers together with the slow carrier relaxation between quantum well and quantum dots lead to a population bottleneck that causes considerable build-up of quantum-well population. Comparison of the two curves in Fig. 4(a) clearly shows a large difference between quantum well and quantum dots in the rate of carrier density increase. Second, in contrast to quantum-well or bulk lasers, many-body effects in a quantum-dot structure are more dependent on nonlasing states than lasing states [32]. This is because in a quantum-dot structure, the lasing states are discrete, and therefore, are more limited in coupling via the Coulomb interaction. The net result is a bandgap renormalization that is largely unchecked by population clamping.

Upon termination of the current pulse, the carrier densities in the different regions begin to decrease. This reverses the bandgap renormalization, which causes the laser frequency to move toward gain peak. The gain continues to be above the CW value because of the influx of carriers stored in the quantum well into the quantum dots. As long as the increase in gain due to the shift toward gain peak exceeds the decrease in gain due to depletion of carriers in the quantum dots, the laser output increases. The second intensity peak occurs where the two processes balance each other. Thereafter, the laser output decreases to its CW value.

Several features visible in Fig. 4 illustrate the nonequilibrium character of laser behavior. The sharp dip in quantum-dot carrier density at $t \approx 100$ ps is a consequence of the plasma heating as discussed earlier. The abrupt increase and decrease in the bulk carrier density [Fig. 4(b)], showing the extent to which the bulk population can follow the current pulse, and their absence in the quantum-well and quantum-dot curves in Fig. 4(a) suggests that the carriers in the different regions are not in equilibrium with one another. Last, the lack of population clamping indicates the presence of kinetic holes.

In Fig. 5, the solid curves depict the kinetic holes in the quantum-dot electron population at different times and the dashed curves show the normal distribution $\rho(\varepsilon)$ used to represent the spectral distribution of the inhomogeneously broadened quantum-dot states. Fig. 5(a) shows the presence of a broad kinetic hole in the carrier distribution due to the CW lasing and prior to the current pulse. A population shift toward lower energy is clearly visible by comparing the solid and dashed curves. This shift is a consequence of the higher population in the lower energy states in the inhomogeneous distribution. During the pulse, there is an the overall red shift of the dot states and a transient vanishing of the kinetic hole. This is illustrated in Fig. 5(b), which depicts the quantum-dot electron distribution at the time when the detuning is maximum, and consequently, the laser output is minimum. Also at this time, the gain has dropped below the lasing threshold value. Fig. 5(c) is a plot of the quantum-dot electron population distribution at $t = 280$ ps, which is at the second output maximum. Now, a deep hole is again burned close to the center of the carrier distribution.

IV. Gain Switching

Gain switching is a good example of an experimental situation where nonequilibrium effects are likely to be present. Fig. 6 shows the time evolution of output intensity for the laser considered in the previous sections, when a $J = 2$ kA/cm^2 injection current is applied at $t = 0$. The two curves illustrate the dependence of the quantum-dot laser switch-on behavior on

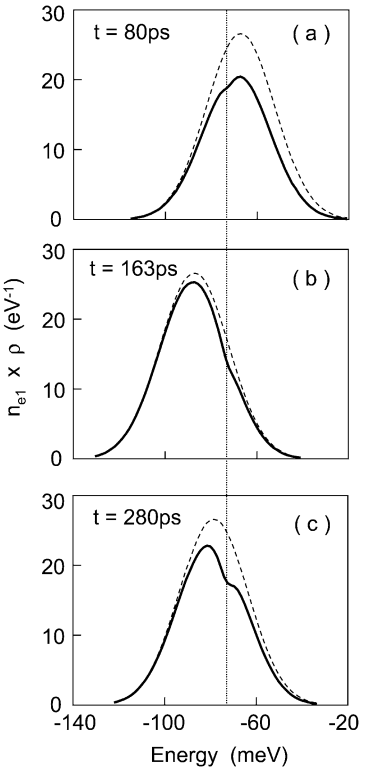

Fig. 5. Quantum-dot electron populations (solid curves) at times (a) $t = 80$ ps, (b) 163 ps, and (c) 280 ps. For reference, the dashed curve is the inhomogeneous quantum-dot state distribution.

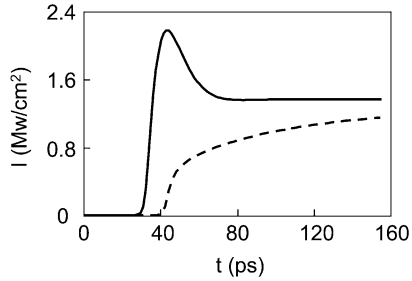

Fig. 6. Laser switch-on behaviors for shallow (solid curve) and deep (dashed curve) quantum dots.

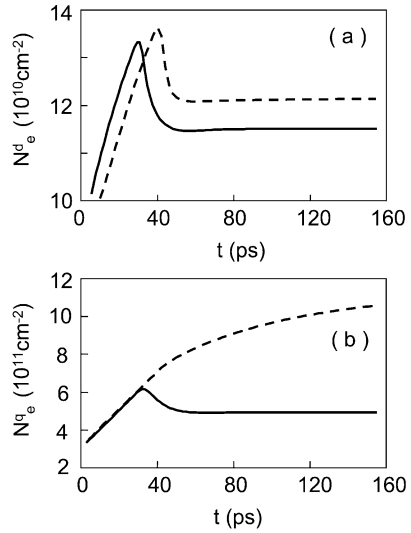

Fig. 7. Time dependence of (a) quantum-dot and (b) quantum-well electron densities for shallow (solid curve), and deep (dashed curve) quantum dots.

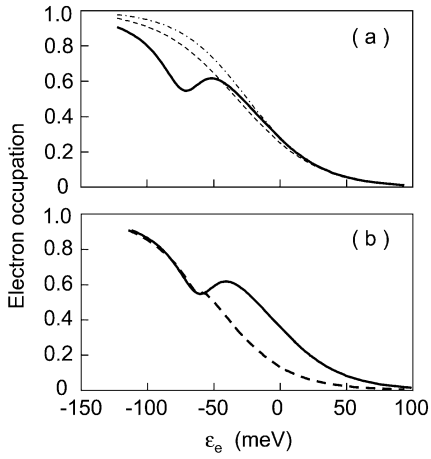

Fig. 8. (a) Electron occupation versus energy for deep quantum dots. The solid curve is the actual distribution n_{e1}, the dashed and dotted-dashed curves are the Fermi–Dirac functions $f(\varepsilon, \mu_e^{(3)}, T_p)$ and $f(\varepsilon, \mu_e^{(3l)}, T_l)$. (b) Electron occupation n_{e1} versus energy for shallow (dashed curve), and deep (solid curve) quantum dots.

scattering rates. Rates for relaxation within quantum-dot states, as well as relaxation and capture between quantum-dot and quantum-well states have be obtained from quantum-kinetic calculations [18], [19]. The results indicate that these rates can vary over an order of magnitude, depending on experimental conditions. In this section, we use two sets of relaxation rates that represent the upper and lower limits. We consider the case of weakly confined quantum dots, e.g., $In_{0.3}Ga_{0.7}As$ quantum dots in a GaAs quantum well, (henceforth, referred to as shallow-dot case), where relaxation rates are typically in the high range of $\gamma_{c-c}^{(3)} = 2 \times 10^{12}$ s^{-1} and $\gamma_{c-p}^{(3)} = 10^{12}$ s^{-1} [36]. Also, we consider the case of strongly confined quantum dots, e.g., InAs quantum dots in a $In_{0.3}Ga_{0.7}As$ quantum well, (deep-dot case), where the relaxation rates are typically in the low range of $\gamma_{c-c}^{(3)} = 2 \times 10^{11}$ s^{-1} and $\gamma_{c-p}^{(3)} = 10^{11}$ s^{-1} [36]. In Fig. 6, the solid and dashed curves correspond to the shallow and deep dot cases, respectively.

One factor causing the difference in dynamical behavior, specifically the absence of a gain-switch peak with the deep dots, is the difference in coupling between quantum-well and quantum-dot populations. For the shallow-dot case, both quantum-dot and quantum-well populations directly support the lasing transition. One sees this from the solid curves Fig. 7(a) and (b), showing that population overshoot and clamping in the quantum-dot and quantum-well populations are synchronized. In contrast, the dashed curves in Fig. 7(a) and (b) indicate that the quantum-well and quantum-dot population dynamics are largely decoupled for the deep-dot case. The slower but more constant influx of carriers from the quantum well to the quantum dots damps the relaxation oscillation necessary for a gain-switch spike to occur.

Further evidence of differences in the extent of nonequilibrium effects may be seen in Fig. 8(a). The solid curve shows the energy dependence of the actual electron population in the entire gain structure for the deep-dot situation at time $t > 80$ ps,

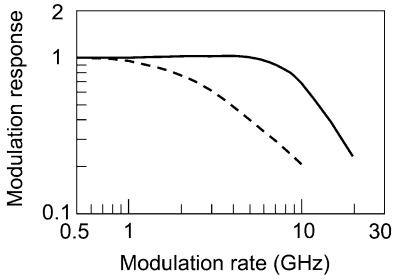

Fig. 9. Quantum-dot laser modulation response for shallow (solid curve), and deep (dashed curve) quantum dots.

which is after steady state is reached. The energy is referenced to the unexcited quantum-well bandedge. Clearly visible is a kinetic hole within the inhomogeneous quantum-dot distribution and centered at the laser energy. Also plotted are the asymptotic Fermi–Dirac distributions $f(\varepsilon, \mu_e^{(3)}, T_p)$ and $f(\varepsilon, \mu_e^{(3l)}, T_l)$ reached via carrier–carrier and carrier–phonon collisions, respectively. Differences between the solid and dashed curves indicate deviations from quasi-equilibrium conditions, and differences between the dashed and dot-dashed curves indicate the extent of plasma heating. The pronounced spectral hole indicates considerable gain saturation. Fig. 8(b) compares the electron populations for the two different quantum-dot structures. The difference between the curves, especially at the high energy side of the laser energy, indicates the significant difference in the number of carriers contributing to the lasing transition in the two cases. Both spectral holes have basically identical depth, but the hole width is much wider for the high relaxation rate case. Carriers outside the spectral hole do not contribute to the laser transition. Therefore, the narrower spectral hole in the calculations for the deep-dot case means that less carriers are available to support a gain-switched pulse.

V. Modulation Response

As discussed in the introduction, a challenge for the theory is to describe the dynamical response of a quantum-dot laser over a continuous band of modulation frequencies, ranging from where the rate equation approximation is valid to where nonequilibrium effects are present. The curves in Fig. 9 demonstrate the ability of the present theory to meet this challenge. They are computed using a sinusoidally varying injection current

$$J(t) = (1 - \delta) + \delta \cos(\Omega t). \tag{37}$$

The laser modulation response at frequency Ω is the difference between the maximum and minimum laser intensities, with the low frequency response normalized to unity. Limiting ourselves to the linear regime, we consider a small modulation depth of $\delta = 0.1$.

Assuming laser operation at five times above threshold and considering the same two quantum-dot structures as in the previous section, we obtain the modulation response curves shown in Fig. 9. The solid curve is for the shallow-dot (faster relaxation rates) case, while the dashed curve is for the deep-dot (slower relaxation rates) case. For the shallow dots, the modulation response remains relatively flat up to 10 GHz and then

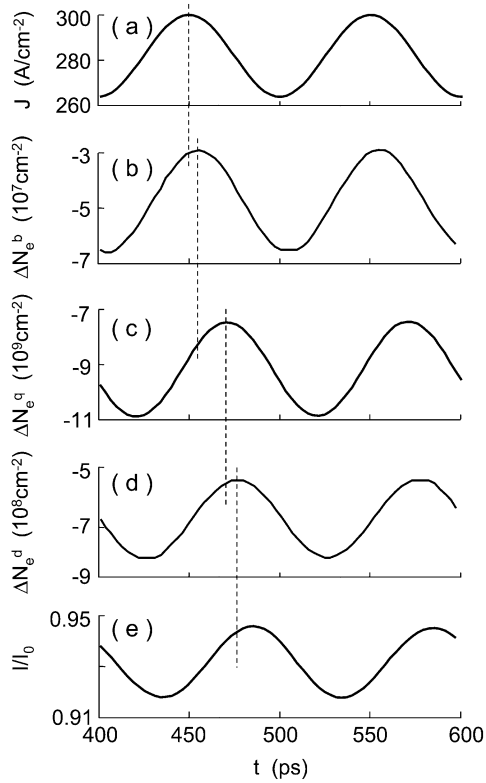

Fig. 10. (Top to bottom) Time dependence of (a) injection current, (b) bulk, (c) quantum-well, and (d) quantum-dot electron densities, and (e) laser intensity for deep quantum dots. The dashed lines indicate the successive time delays between the various properties.

drops off sharply. Unlike a typical bulk and quantum-well laser modulation response, there is strong damping of relaxation oscillations, resulting in the absence of a peak in the modulation response curve at the relaxation oscillation frequency. We find the bandwidth and damping to be relatively strongly depend on the confinement factor. Dynamical performance is limited by the a small modal differential gain due to a low dot density, suggesting the importance of gain saturation (gain compression) effects, consistent with the explanation given for recent experimental results [1], [2]. As is the case with gain switching, nonequilibrium effects are negligible for this shallow-dot structure, with the carrier populations over the entire modulation bandwidth relatively well approximated by Fermi–Dirac distributions.

The dashed curve in Fig. 9 shows that for the deep dots, the modulation response degrades appreciably past 1 GHz. Like the shallow-dot case, dynamical performance is limited by gain saturation. However, additionally, time varying spectral holes are present in both electron and hole populations, indicating the presence of nonequilibrium effects. The situation is very similar to that described in Fig. 8. The slow quantum-dot relaxation gives rise to a lag in response of the quantum-dot electron and hole populations to the injection current variation. This may be seen in Fig. 10, which shows the time dependences of electron densities in the different regions for a 10-GHz modulation frequency. Fig. 10(a) and (b) demonstrate that the barrier electron density directly follows the current modulation. However, the response of the quantum-dot and quantum-well

electron densities lags noticeably, as is evident by comparing Fig. 10(c) and (d) to (b). The relatively large delay (separation of the density maxima) of approximately 20 ps indicates a problem in effectively transmitting temporal information from the injection current to the quantum-well and quantum-dot populations. Fig. 10(e) shows the modulated laser output, which is noticeably out of sync with the injection current.

VI. Conclusion

In summary, nonequilibrium effects can play an important role in the semiconductor quantum-dot laser dynamical behavior because scattering rates involving quantum-dot states may be relatively slow. To describe such effects, we presented and evaluated a theory, where the time evolutions of the laser field and quantum-dot gain medium are described according to the Maxwell–semiconductor–Bloch equations. Many-body Coulomb effects are included at the level of the screened Hartree–Fock approximation, and the relaxation and capture of carrier populations due to carrier–carrier and carrier–phonon collisions are treated in the effective relaxation rate approximation. Examples are presented that demonstrate the capabilities of the theory in describing the effects of population transfer between different regions of the heterostructures, spectral hole burning in the inhomogeneous quantum-dot distributions, and plasma heating.

References

[1] S. Ghosh, S. Pradhan, and P. Bhattacharya, "Dynamic characteristics of high-speed $In_{0.4}Ga_{0.6}As$/GaAs self-organized quantum dot lasers at room temperature," *Appl. Phys. Lett.*, vol. 81, pp. 3055–3057, 2002.

[2] S. M. Kim, Y. Wang, M. Keever, and J. S. Harris, "High-frequency modulation characteristics of 1.3-μm InGaAs quantum-dot lasers," *IEEE Photon. Technol. Lett.*, vol. 16, no. 2, pp. 377–379, Feb. 2004.

[3] R. Nagarajan, M. Ishikawa, T. Fukushima, R. Geels, and J. E. Bowers, "High speed quantum wlll lasers and carrier transport effects," *IEEE J. Quantum Electron.*, vol. 28, no. 10, pp. 1990–2008, Oct. 1992.

[4] M. Grupen and K. Hess, "Simulation of carrier transport and nonlinearities in quantum-well laser diodes," *IEEE J. Quantum Electron.*, vol. 34, no. 1, pp. 120–140, Jan. 1998.

[5] K. Y. Lau, "Dynamics of quantum well lasers," in *Quantum Well Lasers*, P. S. Zory Jr., Ed. Boston, MA: Academic, 1993, ch. 5.

[6] P. Bhattacharya, D. Klotzkin, O. Qasaimeh, W. Zhou, S. Krishna, and D. Zhu, "High-speed modulation and switching characteristics of In(Ga)As–Al(Ga)As self-organized quantum-dot lasers," *IEEE J. Select. Topics Quantum Electron.*, vol. 6, no. 3, pp. 426–438, May–Jun., 2000.

[7] P. Borri, W. Langbein, J. M. Hvam, F. Heinrichsdorff, M.-H. Mao, and D. Bimberg, "Spectra hole-burning and carrier-heating dynamics in InGaAs quantum-dot amplifiers," *IEEE J. Select. Topics Quantum Electron.*, vol. 6, no. 3, pp. 544–551, May–Jun. 2000.

[8] M. Grundmann and D. Bimberg, "Theory of random population for quantum dots," *Phys. Rev. B*, vol. 55, pp. 9740–9745, 1997.

[9] H. Benisty, C. M. Sotomayor-Torres, and C. Weisbuch, "Intrinsic mechanism for the poor luminescence properties of quantum-box systems," *Phys. Rev. B.*, vol. 44, pp. R10945–R10948, 1991.

[10] M. Sugawara, K. Mukai, and H. Shoji, "Effect of phonon bottleneck on quantum-dot laser performance," *Appl. Phys. Lett.*, vol. 71, pp. 2791–2793, 1997.

[11] H. Yokoyama and S. D. Brorson, "Rate equation analysis for semiconductor microcavity lasers," *J. Appl. Physics*, vol. 66, pp. 4801–4805, 1989.

[12] F. Adler, M. Geiger, A. Bauknecht, F. Scholz, H. Schweizer, M. H. Pikuhn, B. Ohnesorge, and A. Forchel, "Optical transitions and carrier relaxation in self assembled InAs/GaAs quantum dots," *J. Appl. Phys.*, vol. 80, pp. 4019–4026, 1996.

[13] J. E. Bowers, B. R. Hemenway, A. H. Gnauck, and D. P. Wilt, "High-speed InGaAsP constricted-mesa lasers," *IEEE J. Quantum Electron.*, vol. QE-22, no. 6, pp. 833–844, Jun. 1986.

[14] A. Markus and A. Flore, "Modeling carrier dynamics in quantum-dot lasers," *Phys. Stat. Sol. A*, vol. 201, pp. 338–344, 2004.

[15] F. Rossi, S. Hass, and T. Kuhn, "Ultrafast relaxation of photoexcited carriers: The role of coherence in the generation process," *Phys. Rev. Lett.*, vol. 72, pp. 152–155, 1994.

[16] R. Binder and S. W. Koch, "Non-equilibrium semiconductor dynamics," *Prog. Quantum Electron.*, vol. 19, pp. 307–460, 1995.

[17] A. Knorr, S. Hughes, T. Stroucken, and S. W. Koch, "Theory of ultrafast spatio-temporal effects in semiconductor heterostructures," *J. Chem. Phys.*, vol. 210, pp. 27–47, 1996.

[18] T. R. Nielsen, P. Gartner, and F. Jahnke, "Many-body theory of carrier capture and relaxation in semiconductor quantum-dot lasers," *Phys. Rev. B.*, vol. 69, pp. 235 314–235 326, 2004.

[19] H. C. Schneider, W. W. Chow, and S. W. Koch, "Excitation induced dephasing in semiconductor quantum dots," *Phys. Rev. B*, vol. 70, pp. 235 308–235 311, 2004.

[20] F. Jahnke and S. W. Koch, "Theory of carrier heating through injection pumping and lasing in semiconductor microcavity lasers," *Opt. Lett.*, vol. 18, pp. 1438–1440, 1993.

[21] S. W. Koch, F. Jahnke, and W. W. Chow, "Physics of semiconductor microcavity lasers," *Semicond. Sci. Technol.*, vol. 10, pp. 739–751, 1995.

[22] W. W. Chow and S. W. Koch, *Semiconductor-Laser Fundamentals: Physics of the Gain Materials*. Berlin, Germany: Springer-Verlag, 1999.

[23] J. A. Lott, N. N. Ledenstsov, V. M. Ustinov, A. Yu Egorov, A. E. Zhukov, P. S. Kop'ev, Ah. I. Alferov, and D. Bimberg, "InAs-InGaAs quantum dot VCSELs on GaAs substrates emitting at 1.3 μm," *Electron. Lett.*, vol. 36, pp. 1384–1385, 2000.

[24] M. Grundmann, "Feasibility of 5 Gbit/s wavelength division multiplexing using quantum-dot lasers," *Appl. Phys. Lett.*, vol. 77, pp. 4265–4267, 2000.

[25] U. Bockelmann and T. Egeler, "Electron relaxation in quantum dots by means of Auger processes," *Phys. Rev. B.*, vol. 46, pp. 15 574–15 577, 1992.

[26] U. Bockelmann and G. Bastard, "Phonon scattering and energy relaxation in two-, one-, and zero-dimensional electron gases," *Phys. Rev. B.*, vol. 42, pp. 8947–8951, 1990.

[27] W. W. Chow, H. C. Schneider, S. W. Koch, C. H. Chang, L. Chrostowski, and C. J. Chang-Hasnain, "Nonequilibrium model for semiconductor laser modulation response," *IEEE J. Quantum Electron.*, vol. 38, no. 4, pp. 402–409, Apr. 2002.

[28] A. Thränhardt, S. Becker, C. Schlichenmaier, I. Kuznetsova, T. Meier, S. W. Koch, J. Hader, J. V. Moloney, and W. W. Chow, "Nonequilibrium gain in optically pumped GaInNAs laser structures," *Appl. Phys. Lett.*, vol. 85, pp. 5526–5528, 2004.

[29] K. Kim, J. Urayama, T. B. Norris, J. Singh, J. Phillips, and P. Bhattacharya, "Gain dynamics and ultrafast spectral hole burning in In(Ga)As self-organized quantum dots," *Appl. Phys. Lett.*, vol. 81, pp. 670–672, 2002.

[30] P. Miska, J. Even, C. Paranthoen, O. Dephasese, H. Folliot, S. Loualiche, M. Senes, and X. Marie, "Optical properties and carrier dynamics of InAs/InP(113)B quantum dots emitting between 1.3 and 1.55 μm for laser applications," *Physica E*, vol. 17, pp. 56–59, 2003.

[31] H. D. Summers, D. R. Matthews, P. M. Smowton, P. Rees, and M. Hopkinson, "Laser dynamics in self-pulsating quantum dot systems," *J. Appl. Phys.*, vol. 95, pp. 1036–1041, 2004.

[32] H. C. Schneider, W. W. Chow, and S. W. Koch, "Many-body effects in the gain spectra of highly excited quantum-dot lasers," *Phys. Rev. B.*, vol. 64, pp. 115 315–115 321, 2001.

[33] H. Haug and S. W. Koch, *Quantum Theory of the Optical and Electronic Properties of Semiconductors*, 4th ed, Singapore: World Scientific, 2004.

[34] W. W. Chow and H. C. Schneider, "Theory of laser gain in InGaN quantum dots," *Appl. Phys. Lett.*, vol. 81, pp. 2566–2568, 2002.

[35] W. W. Chow, A. F. Wright, A. Girndt, F. Jahnke, and S. W. Koch, "Microscopic theory of gain for InGaN/AlGaN quantum well laser," *Appl. Phys. Lett.*, vol. 71, pp. 2608–2610, 1997.

[36] W. W. Chow, D. Haffaker, and H. C. Schneider, "Dephasing effects on laser gain in shallow and deep semiconductor quantum dots," in *Proc. IEEE 19th Int. Semiconductor Laser Conf.*, Matsue, Japan, Sep. 2004.

Weng W. Chow received the Ph.D. degree in physics from the University of Arizona, Tucson. His dissertation work involved fluctuation phenomena in quantum optics.

He was an Associate Professor of Physics and Astronomy at the University of New Mexico before joining Sandia National Laboratories, Albuquerque, NM, where he is a Distinguished Member of the Technical Staff. His primary research interest is in the application of microscopic theory to semiconductor laser device development. Some of this work is described in two texts, *Semiconductor-Laser Physics* (New York: Springer-Verlag, 1997) and *Semiconductor-Laser Fundamentals: Physics of the Gain Materials* (New York: Springer-Verlag, 1999). His other interests include laser gyros, phased arrays, coupled lasers, quantum optics and optical ignition of pyrotechnics. He is an Adjoint Professor of Optical Sciences at the University of Arizona, and an Honorary Professor of Physics at Cardiff University, Cardiff, Wales, U.K.

Prof. Chow is a fellow of the Optical Society of America. He received the 1998 Department of Energy Basic Energy Science/Material Science Award and an 2003 Alexander von Humboldt Forschungspreise.

Stephan W. Koch received the M.S. and Ph.D. degrees in physics from Goethe University, Frankfurt, Germany, in 1977 and 1979, respectively.

He has been a Professor of Physics at Philipps-University, Marburg, Germany, and a Research Professor at the Optical Sciences Center, University of Arizona, Tucson, since 1993. He spent eight years, first as an Associate Professor, then as a Professor of Physics and Optical Sciences, with the University of Arizona. He was a Heisenberg Fellow at the University of Frankfurt, Frankfurt, Germany, in 1985, and a Visiting Scientist at IBM Research in 1981 and 1983. He is the author or coauthor of six books, editor of one book, and author or coauthor of more than 400 publications in refereed scientific journals. He was a Divisional Associate Editor of *Physics Review Letters* from 1997 to 2000, a Topical Editor of *Zeitschrift für Physik* in 1997, and has been a Topical Editor of the *European Physics Journal* since 1998. His fields of research interest include condensed matter theory, optical and electronic properties of semiconductors, many body-interactions, disorder effects, quantum confinement in solids, coherent and ultrafast phenomena, semiconductor laser theory, microcavity effects, and optical instabilities and nonlinearities.

Prof. Koch received the Max-Planck Research Prize in 1999 and the Leibniz Prize of the Deutsche Forschungsgemeinschaft in 1997.